Transverse Coupled Cavity VCSELs: Bridging Ultrabroadband Dynamics to Optical Supermodes

Transverse Coupled Cavity VCSELs: Bridging Ultrabroadband Dynamics to Optical Supermodes

Martino D'Alessandro, *Member, IEEE*, Valerio Torrelli, Francesco Bertazzi, Michele Goano, *Senior Member, IEEE*, Nikolay N. Ledentsov, *Senior Member, IEEE*, Markus Lindemann, Mariangela Gioannini, *Member, IEEE*, Pierluigi Debernardi, and Alberto Tibaldi, *Member, IEEE*

***Abstract*—In this work we investigate the ultrabroadband dynamics of transverse coupled cavity VCSELs. This study is based on a multimode rate equation model, whose parameters are directly provided by a full-wave vectorial electromagnetic solver. This approach sets a step towards the comprehensive physics-based modeling of transverse-coupled cavity VCSELs, providing a relation between the features of the optical supermodes and the enhancements of the intensity modulation response. The approach emphasizes how the bandwidth enhancement, ascribable to a photon-photon resonance picture, can be triggered by forcing asymmetries in the bias and modulation contacting scheme of the device, and the importance of collecting the fields from each single cavity, providing an interpretation of recent experimental observations and paving the way towards more systematic design strategies.**

***Index Terms*—High-speed data communications, VCSELs, optical mode solvers, multimode rate equations, transverse coupled cavities.**

I. Introduction

OPTICAL transceivers designed for intradatacenter communications are currently pushing the boundaries to consolidate 200 Gbps data rates, and look forward, envisioning 800 Gbps Ethernet tranceivers [1]. Focusing on the optical light source of the transmission block, vertical-cavity surface-emitting lasers (VCSELs) have emerged as one of the most promising choices for high-speed low-power data communications, thanks to their compact active region, sub-mA threshold currents, and optimal packaging and coupling with optical fibers due to their circular symmetry [2], [3], [4], [5]. While 100 Gbps bitrates can be already achieved with a combination of state-of-the-art lasers [6], [7], complex modulation techniques such as 4- or even 8-level pulse amplitude modulation (PAM) supported by advanced nonlinear equalization techniques [8], [9], [10], [11], the feeling is that overcoming 200 Gbps is going to require redefining the concept of high-speed VCSELs [12]. In this view, one of the hottest research topics is that of transverse coupled cavity VCSELs (TCC-VCSELs).

While a standard VCSEL resonator consists of a single cavity, TCC-VCSELs feature two or more cavities that are transversely coupled or connected. By properly designing such resonators, it is possible to achieve a huge broadening of the intensity modulation (IM) bandwidth. Several TCC-VCSEL concepts have been presented in the literature over the last ten years, ranging from bowtie devices from the group of prof. Koyama [13], to the vertically-coupled and photonic-crystal VCSELs from the group of prof. Choquette [14], [15], to the very recent daisy-like VCSELs from Optelligence [16].

The ultrabroadband operation of TCC-VCSELs has been described based on analogies with diverse models. The seminal papers by the group of prof. Koyama treat the effect of one of the lateral cavity as a feedback [17], with a model similar to that proposed by Lang and Kobayashi [18]. Successively, these models have been extended, removing the hypothesis of moderate feedback [19], on the basis of a strong experience on edge-emitting lasers [20], [21], [22], and ultimately to the case of many transverse cavities [23]. A different interpretation has been proposed by the group of prof. Choquette [15], which describes the interaction of the two cavities as if there is a driving cavity, controlling through injection locking a secondary one. Although apparently different, all these ideas share a common denominator, namely that: IM bandwidth enhancement can be achieved by technologically implementing a VCSEL featuring two or more phase-shifted fields, in partial analogy with the idea of photon-photon resonance (PPR), consolidated in the context of edge-emitting lasers [24], [25], [26], [27], [28], [29].

It is very likely that the aforementioned perspectives, mainly focused on the TCC-VCSEL carrier and photon dynamics, are all reasonable. Yet, all of them are based on the hypothesis of having a *main* cavity and a *secondary* one, aimed at introducing

Manuscript received 11 December 2023; revised 25 February 2024; accepted 28 February 2024. Date of publication 5 March 2024; date of current version 8 April 2024. This work was supported in part by Cisco Systems, Inc., under the Sponsored Research Agreement MultiVCSEL, and in part by the European Union under two initiatives of the Italian National Recovery and Resilience Plan (NRRP) of NextGenerationEU: the partnership on *Telecommunications of the Future* (PE00000001 – program "RESTART"), and the National Centre for HPC, Big Data and Quantum Computing (CN00000013 – CUP E13C22000990001). *(Corresponding author: Alberto Tibaldi.)*

Martino D'Alessandro, Valerio Torrelli, Francesco Bertazzi, Michele Goano, and Alberto Tibaldi are with the Department of Electronics and Telecommunications, Politecnico di Torino, 10129 Turin, Italy, and also with the Consiglio Nazionale delle Ricerche (CNR), Istituto di Elettronica e di Ingegneria dell'Informazione e delle Telecomunicazioni (IEIIT), 10129 Turin, Italy (e-mail: alberto.tibaldi@polito.it).

Mariangela Gioannini is with the Department of Electronics and Telecommunications, Politecnico di Torino, 10129 Turin, Italy.

Pierluigi Debernardi is with the Consiglio Nazionale delle Ricerche (CNR), Istituto di Elettronica e di Ingegneria dell'Informazione e delle Telecomunicazioni (IEIIT), 10129 Turin, Italy.

Nikolay N. Ledentsov is with the VI-Systems GmbH, 10623 Berlin, Germany.

Markus Lindemann is with the Ruhr-Universität Bochum, Photonics and Terahertz Technology, Universitätstr. 150, 44801 Bochum, Germany.

Digital Object Identifier 10.1109/JPHOT.2024.3373171

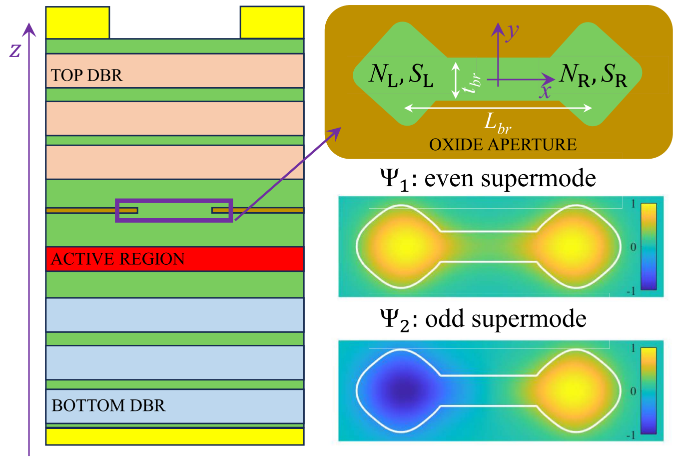

Fig. 1. Left: sketch of the epitaxy of the device under investigation. The red layer indicates the active QW region, the light blue and red rectangles denote the bottom (n-doped) and top (p-doped) DBRs, the brown layer indicates the oxide and the yellow rectangles are the contacts. Right: top view of the bow-tie shaped oxide aperture. Bottom right: plot of the computed even and odd optical supermodes supported by this geometry.

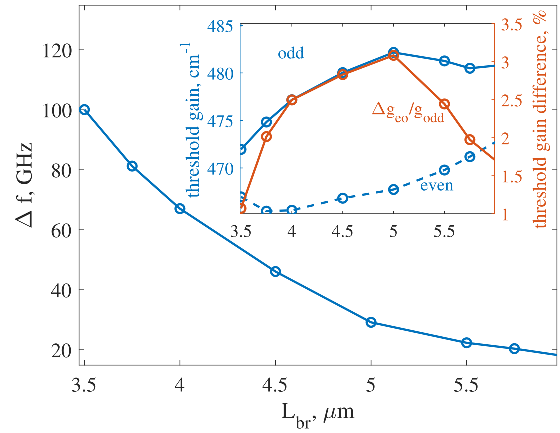

Fig. 2. Frequency separation between the even and odd optical supermodes as a function of the bridge length for $t_{\rm br} = 1.2$ μm, together with their threshold gain per QW.

interference effects with the main one. To the best of our understanding, this vision could struggle with mode solvers, which treat TCC-VCSELs as a whole resonator. Recent works appear to step towards this direction, as demonstrated by the thorough investigations of supermode dynamics in VCSEL arrays [30], [31], or by the fact that TCC-VCSEL dynamics could result from the interaction of two (super)modes, rather than from two different coupled devices [32].

To the best of our knowledge, the modeling chain is still lacking a ring connecting the modal features of TCC-VCSELs and the carrier dynamics related to them. In this view, the scope of this paper is to present a modal analysis of the ultrabroadband operation of TCC-VCSELs.

The paper is structured as follows. Section II presents a description of the TCC-VCSEL under study, introducing its optical modes features. In Section III, a rate equation for the dynamics of the device under study is derived and in Section IV its broadband operation is numerically proven and interpreted.

II. Device Under Investigation

The TCC-VCSEL under study is inspired by the structure manufactured in [33], and is sketched in Fig. 1. Here, the left part of the figure reports a qualitative cross-section, which is substantially identical to that of a typical AlGaAs *pin* VCSEL. The active region, indicated in red, is composed by four GaAs quantum wells (QW), optimized for 850 nm emission. These are embedded within a cavity defined by two distributed Bragg reflectors (DBRs), the top (p-doped, light red rectangles) and bottom (n-doped, light blue rectangles) including 21 and 35 pairs, respectively. The yellow regions indicate the contacts. In particular, the bottom ground contact is connected to the n-doped DBR, while the top contact, above the p-doped DBR, is used to inject current. Just like in the majority of AlGaAs VCSELs, the cavity includes an oxide layer, indicated in brown, whose aperture can be engineered to control the current injection in the active region and the transverse optical confinement. While in *standard* VCSELs the oxide aperture is circular or elliptical, the peculiarity of this TCC-VCSEL is to have an oxide aperture like the one reported in the top-right of Fig. 1. This consists of two apertures, linked by a central, narrower straight semiconductor region, from here on referred to as *bridge*. We define the bridge length $L_{\rm br}$ as the distance between the centers of the two apertures and $t_{\rm br}$ as the thickness of the bridge along the y direction. Typical values for $L_{\rm br}$ and $t_{\rm br}$ are 5 μm and 1.2 μm respectively. The electromagnetic investigation of the device is performed by means of our in-house Vcsel ELectroMagnetic Suite VELMS [34], [35] which, starting from the description of the 3-dimensional refractive index profile, can calculate the VCSEL modes together with their emission frequencies, their longitudinal confinement factor and their threshold gains. As a consequence of its peculiar oxide geometry, in place of a unique fundamental mode, the TCC-VCSEL under study features two *supermodes*, *i.e.*, modes whose topographies are simultaneously nonvanishing in both apertures, as in the examples reported in the bottom-right part of Fig. 1. The generation of supermodes is intuitively ascribable to the interaction of the two apertures defined by the oxide shape. The localized modes of the single cavities combine, leading to even and odd field topographies extended over the whole cross section, as explained by coupled-mode theory [36]. The mode characterized by lower threshold gain and higher emission frequency features an odd symmetry, while the other one features an even symmetry. Typical values of the frequency detuning Δf are of the order of tens of GHz, while the threshold gain difference $\Delta g_{\rm eo}$ is about a few percent of the average threshold gain. The electromagnetic structure of the VCSEL can be optimized to engineer Δf and $\Delta g_{\rm eo}$. As a preliminary example, Fig. 2, the frequency separation between the even and odd supermodes is reported for a varying bridge length, together with their threshold gain per QW. It can be seen that it is possible to solely tune Δf without affecting $\Delta g_{\rm eo}$ by shortening the distance between the centers of the two apertures. In this way, it is possible to reach frequency separations as high as 100 GHz, while the threshold gain splitting remains around $1 \div 3$ percent.

III. Rate Equation Model for TCC-VCSELs

One of the targets of this work is to interpret and describe the ultra broadband operation of TCC-VCSELs by means of a rate equation model, whose input parameters can be directly related to the outputs of an electromagnetic mode solver. Rate equation models consist of two fundamental constituents: field rate equations, describing the dynamics of the photon populations for each VCSEL mode, and carrier rate equations, providing a model of the charge injection in the active region. Focusing on the former, a rate equation for each i-th mode field amplitude can be formulated by expanding the electric field in the optical wave equations on the basis of the cavity modes (see Appendix A for details), obtaining:

$$\frac{\mathrm{d}E_i}{\mathrm{d}t} = \left[-\frac{1}{2\tau_{\mathrm{p}i}} + \mathrm{i}\Delta\omega_i\right] E_i + \sum_{j=1}^{N_\mathrm{m}} k_{ij} E_j, \tag{1}$$

where, with reference to the i-th mode, $E_i(t)$ is the complex amplitude, $\tau_{\mathrm{p}i}$ is the photon lifetime, and $\Delta\omega_i$ is the frequency difference with respect to an (arbitrary) reference frequency. The factor k_{ij} can be computed by evaluating the gain-field overlap integrals over the active region (17). In particular, the terms $i = j$ represent the modal gains, while the terms $i \neq j$ represent the cross-coupling terms between the different modes. In this work, we restrict our basis to the sole even and odd modes ($N_\mathrm{m} = 2$), whose threshold gain is much lower than the other ones. In order to achieve a lumped model, the carrier and photon densities are considered piece-wise constant in the two coupled cavities as indicated in Fig. 1. Also, aiming to privilege the model simplicity, a linear expression for the gain is adopted:

$$g_{\mathrm{l,r}} = \frac{v_\mathrm{g} G_\mathrm{d}}{1 + \epsilon S_{\mathrm{l,r}}} (N_{\mathrm{l,r}} - N_{\mathrm{tr}}), \tag{2}$$

where the subscripts left (l) and right (r) indicate the corresponding apertures, $g_{\mathrm{l,r}}$ is the gain, $N_{\mathrm{l,r}}$ is the carrier density, $S_{\mathrm{l,r}}$ is the photon density, G_d is the active region differential gain, N_{tr} is the transparency carrier density, ϵ is the spectral hole burning gain compression factor and v_g is the light velocity divided by the refractive index of the active region n_g.

We introduce the terms w_{ma} as the overlap integral of the mode m with the aperture a. In particular, m could be even (e) or odd (o), while a could be right (r) or left (l), indicating the corresponding aperture. In this work, assuming a perfectly symmetric device we consider:

$$w_{\mathrm{er}} = \frac{1}{\sqrt{2}}, \quad w_{\mathrm{el}} = \frac{1}{\sqrt{2}}, \quad w_{\mathrm{or}} = -\frac{1}{\sqrt{2}}, \quad w_{\mathrm{ol}} = \frac{1}{\sqrt{2}}. \tag{3}$$

Within these assumptions, the integral terms k_{ij} simplify to a linear combination of the left and right gains:

$$k_{\mathrm{ee}} = k_{\mathrm{oo}} = \frac{\Gamma_\mathrm{z}}{4}(1 + \mathrm{i}\alpha_\mathrm{h})(g_\mathrm{r} + g_\mathrm{l}), \tag{4}$$

$$k_{\mathrm{eo}} = k_{\mathrm{oe}} = \frac{\Gamma_\mathrm{z}}{4}(1 + \mathrm{i}\alpha_\mathrm{h})(g_\mathrm{l} - g_\mathrm{r}), \tag{5}$$

where Γ_z is the longitudinal confinement factor and α_h is the linewidth enhancement factor (Henry factor).

Finally, introducing the standard phenomenological rate equations for the carrier density in the right and left apertures, the system becomes:

$$\begin{cases} \partial_t E_\mathrm{o} = -\frac{E_\mathrm{o}}{2\tau_{\mathrm{po}}} + k_{\mathrm{oo}} E_\mathrm{o} + k_{\mathrm{oe}} E_\mathrm{e}, & \text{(6a)} \\ \partial_t E_\mathrm{e} = \left(-\frac{1}{2\tau_{\mathrm{pe}}} + \mathrm{i}\Delta\omega\right) E_\mathrm{e} + k_{\mathrm{eo}} E_\mathrm{o} + k_{\mathrm{ee}} E_\mathrm{e}, & \text{(6b)} \\ \partial_t N_\mathrm{l} = -\frac{N_\mathrm{l}}{\tau_n} - g_\mathrm{l} S_\mathrm{l} + \frac{I_\mathrm{l}}{\mathrm{q}V_\mathrm{a}} - k_{\mathrm{diff}}(N_\mathrm{l} - N_\mathrm{r}), & \text{(6c)} \\ \partial_t N_\mathrm{r} = -\frac{N_\mathrm{r}}{\tau_n} - g_\mathrm{r} S_\mathrm{r} + \frac{I_\mathrm{r}}{\mathrm{q}V_\mathrm{a}} + k_{\mathrm{diff}}(N_\mathrm{l} - N_\mathrm{r}), & \text{(6d)} \end{cases}$$

with:

$$S_\mathrm{l} = |w_{\mathrm{el}} E_\mathrm{e} + w_{\mathrm{ol}} E_\mathrm{o}|^2, \qquad S_\mathrm{r} = |w_{\mathrm{er}} E_\mathrm{e} + w_{\mathrm{or}} E_\mathrm{o}|^2, \tag{7}$$

where E_e and E_o denote the modal amplitude of the even and odd modes respectively, τ_n is the carrier lifetime, k_{diff} is a phenomenological carrier diffusion coefficient, $\Delta\omega$ is the frequency separation of the two modes, and V_a is the active volume.

The model is based on having carrier densities localized in the left and right cavities, and delocalized supermodes. In this view, in order to define the carrier recombination terms related to stimulated emission, it has been necessary to evaluate the photon densities in the left and right cavities, S_l and S_r, appearing in (6c) and (6d), respectively. These two quantities can be interpreted as the photon densities detectable from a narrow-collection-area photodiode aligned only with one of the cavities.

It is useful to express S_l and S_r in terms of the photon densities of the lasing supermode S_{oo}, of the non-lasing supermode S_{ee}, and of a cross-mode contribution S_{eo}, defined as

$$S_{\mathrm{oo}} = |E_\mathrm{o}|^2 \tag{8a}$$

$$S_{\mathrm{ee}} = |E_\mathrm{e}|^2 \tag{8b}$$

$$S_{\mathrm{eo}} = 2\,\mathcal{R}e(E_\mathrm{e} E_\mathrm{o}^*) \tag{8c}$$

Substituting (3) and (8) in (7) it is possible to obtain

$$S_\mathrm{l} = \frac{1}{2}(S_{\mathrm{ee}} + S_{\mathrm{oo}} + S_{\mathrm{eo}}), \qquad S_\mathrm{r} = \frac{1}{2}(S_{\mathrm{ee}} + S_{\mathrm{oo}} - S_{\mathrm{eo}}). \tag{9}$$

The solution of (6) is going to be described, in Section IV, to interpret the broadband operation of TCC-VCSELs. Such equations are quite similar to that used in [27] for studying the multi-mode dynamics of an edge-emitting laser, with the cross-coupling terms k_{ij} arising from the longitudinal gain-field integrals. Also, a similar set of equations has been used in [32] and [15], [37] for studying coupled-cavity VCSELs and coupled photonic crystal apertures respectively, assuming to have two modes, supported from the isolated cavities, which interact through a phenomenological coupling strength. In this work, however, the cross-coupling terms are complex time-dependent quantities which naturally arise from the spatial distribution of the gain. The carrier-induced coupling of the modes is also clear in [38] or in [24], [29], where a similar outcome is shown from a travelling wave formalism.

IV. Broadband Operation

In this section, the ultrabroadband operation of the coupled cavity VCSEL under investigation is numerically proven and

TABLE I
TABLE OF PARAMETERS

Parameter	Value	Unit
ϵ	$3\ 10^{-23}$	m^3
V_a	$2.25\ 10^{-19}$	m^3
Δf	70	GHz
G_d	$1.2\ 10^{-19}$	m^2
k_{diff}	$2.75\ 10^{11}$	Hz
τ_n	0.5	ns
τ_{pe}	1.5	ps
n_g	3.6	
α_h	2	
Γ_z	0.03	
Δg_{eo}	2%	

TABLE II
SYMBOLS AND ABBREVIATIONS

Symbol	Description
$E_{e,o}$	Even/odd mode amplitude
S_{ee}	Even mode photon density
S_{oo}	Odd mode photon density
S_{eo}	Cross photon density
$N_{l,r}$	Left/right carrier density
$I_{l,r}$	Left/right injected current
$S_{l,r}$	Left/right photon density
$g_{l,r}$	Left/right gain
w_{ma}	m-th mode a-th aperture overlap
IMR	Intensity modulation response
PPR	Photon-photon resonance
TCC	Transverse coupled cavity

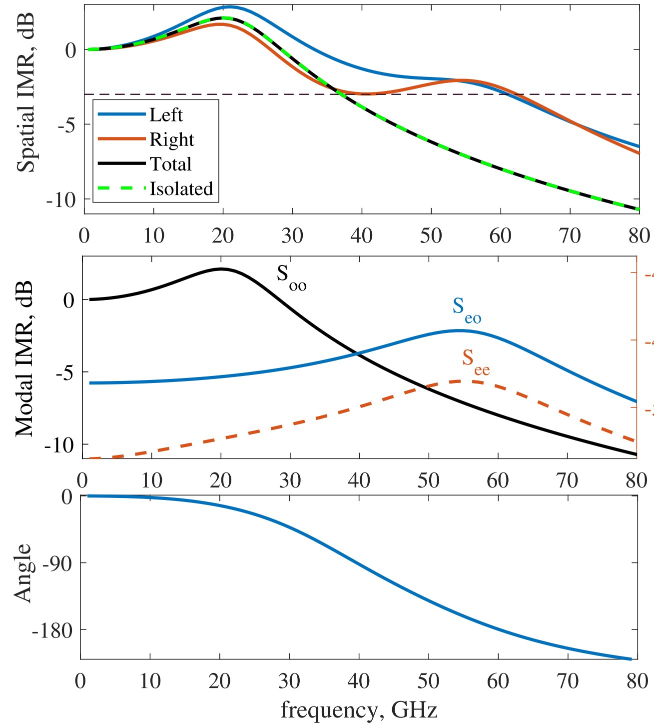

Fig. 3. Top: spatial IMRs for the left (blue), right (red), total (black) and for the isolated cavity photon density (green dashed), obtained for $I_{l,r}$=3 mA, applying the signal solely to the left cavity and normalized to their static values. Middle plot: modal IMRs S_{oo} (black, left axis), S_{eo} (blue, left axis) and S_{ee} (dotted red, right axis) as defined in (8). Bottom: dephasing angle between the right and left photon densities.

interpreted. First, the system of equations derived in Section III is solved with the ordinary differential equation (ODE) tool of MATLAB [39] for static right and left currents I_{l0} and I_{r0}, with the parameters reported in Table I. For the sake of readability, we have also listed all the most relevant symbols in Table II, alongside with their meaning. The intensity modulation response (IMR) can be simulated by superimposing a small current step to I_{l0}, *i.e.,* only in the left cavity, and by evaluating the Fourier transform of the results of the corresponding transient simulation. In this work, we limit our investigation to the symmetric static bias condition, *i.e.*, I_{l0}=I_{r0}. In this case, the continuous wave (CW) regime consists of the odd mode, which has a lower threshold gain, having a much greater amplitude than the even one.

Fig. 3 (top) shows the results for the different definitions of the IMR, normalized to their static (*i.e.*, $\omega = 0$) values, together with the -3 dB level. The solid black line indicates the total IMR, achieved from S_l+S_r. Notably, the green dashed line, corresponding to the IMR of the equivalent single-aperture VCSEL (*i.e.,* removing one of the apertures), is perfectly overlapped with the black curve. The solid blue and red curves are the IMRs of the left and right photon densities, S_l and S_r, respectively, evaluated according to (7). In an experimental setup, these quantities could be obtained by collecting the output power with a properly aligned fiber to the left or right aperture, as described in [33].

It can be noted that S_l and S_r exhibit a peak at a modulation frequency approximately equal to the absolute value of the frequency separation of the modes Δf. This effect, referred to as photon-photon resonance (PPR) [25], [29], almost doubles the $f_{3\,dB}$ of the VCSEL, and therefore improves its high-speed performance. Remarkably, this effect takes place if the light is collected only from one cavity at a time.

This operation can be interpreted by investigating the frequency behaviour of the modal contributions expressed in (9). It appears at a glance that S_{ee}, being related to the non-lasing mode, is about 60 dB below S_{oo}, so that it cannot provide a significant contribution to the IMR. On the other hand, S_{eo} is much larger, and exhibits a peak at about 60 GHz, ascribable to the PPR, at a much higher frequency than the one related to the carrier-photon resonance (about 20 GHz in this device). The effect of S_{eo} is not present in the total response (top panel, black curve) because, as suggested by (9), S_l+S_r leads to a cancellation of the cross-mode coupling.

As described in [33], the time-resolved optical intensities collected from each individual apertures exhibit different behaviors depending on the modulation frequency. In particular, in the CPR regime, the photon densities S_l and S_r are in phase, whereas, in the PPR regime, they are in antiphase. This experiment has been reproduced in Fig. 3 (bottom), which reports the simulated phase shift between S_l and S_r.

At low frequencies, being S_{oo} dominant, (9) suggests that the angle tends to zero. For high frequency, S_{eo} is the dominant term and, therefore, S_r and S_l are in antiphase.

An important point is that the PPR can be observed only if the applied modulation signal is asymmetrical. This can be explained by observing (17): due to the even and odd symmetries

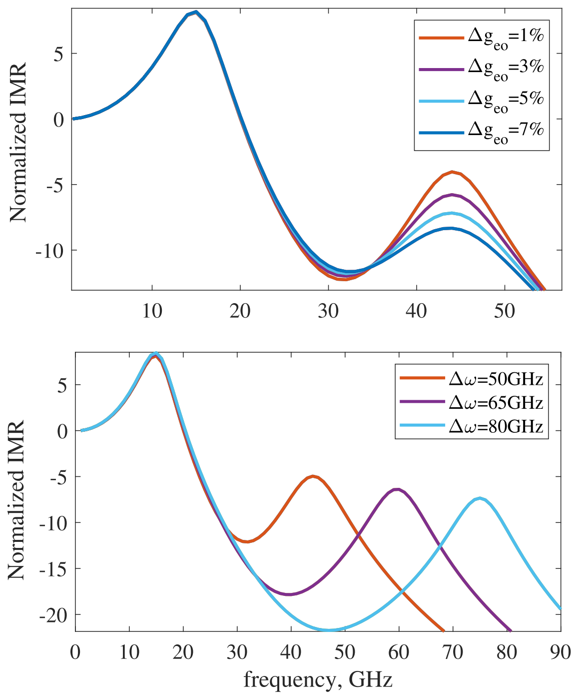

Fig. 4. Top: normalized IMR varying the gain difference of the supermodes. Bottom: normalized IMR varying the frequency difference of the supermodes.

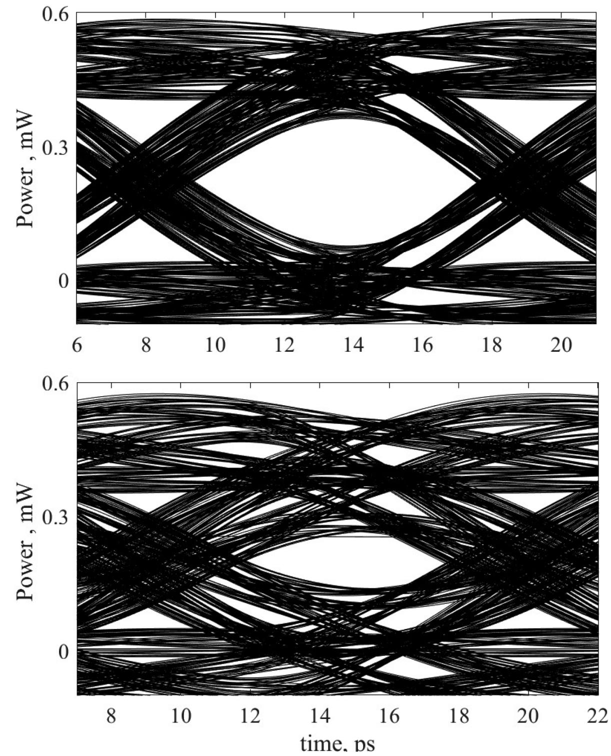

Fig. 5. 90 Gbps PAM-2 eye diagram simulated at the working point of Fig. 3, for equal output logical power levels separation, reported for the coupled cavity device (top) and for the isolated device (bottom). The power is reported with an offset equal to its static low value.

of the considered modes, $k_{\rm eo} = k_{\rm oe} = 0$ for an even distribution of carriers, which would result from a symmetric signal applied to both apertures. In this case, no multi-mode dynamics is triggered since the equations for the various modes are decoupled, and therefore no PPR effect can be observed. This point is a well known aspect of the push-pull modulation schemes, such as the ones described in [40], [41].

The presented model is a useful bridge to link the device-level features to the electromagnetic simulation. Indeed, Fig. 4 (top) shows that the height and broadening of the peak can be engineered by means of the threshold gain separation. Controlling this aspect is fundamental for datacom applications since a too sharp peak would result in a distorted large signal response, while a too low peak would result in a negligible bandwidth enhancement. In Fig. 4 (bottom) instead, it can be seen that the position of the PPR peak can be controlled by Δf, and therefore by the bridge length, as indicated in Fig. 2.

The small-signal analysis performed so far can only provide a qualitative indication regarding the high-speed performance. To actually test the capability of a device for an optical communication application, the *eye diagram* is often adopted as an indicator. In Fig. 5, a 90 Gbps pulse amplitude modulation on two levels (2-PAM) eye diagram is reported for both isolated and coupled cavity case, for an equal photon and current density and for an equal separation of the output logical power levels. The input sequence is a random permutation of all the possible 7 bits combinations. It can be seen that the *eye* is still open only for the TCC device, meaning that the PPR is effective in enhancing the large signal modulation bandwidth. It is to be remarked that the -3 dB bandwidth is a necessary, but not sufficient condition to improve the large-signal dynamics of the device. To this aim, the design should also target a flat IMR.

V. Conclusions and Future Work

In this work, we investigated the connection between the ultra broadband dynamics of TCC-VCSELs and the features of their optical supermodes. The bandwidth enhancement of the TCC-VCSEL device has been explained by means of a physics-oriented model, which starting from the output of an electromagnetic solver provides valuable insights into the experimentally observed phenomena.

Our findings point out that the device under investigation requires further attention and troubleshooting to become viable for industrial production. Specifically, it has been shown that, in the perfect symmetric investigated case, the PPR effect can be observed only in the case individual cavities are probed, requiring a careful alignment with the fiber. Additionally, the requirement for asymmetric applied signal turns into the necessity of the electrical isolation of the apertures, such as the one performed in [37]. Furthermore, the PPR-induced bandwidth enhancement is a direct consequence of the second cavity. Yet, this is paid at the price of a doubled active area, corresponding to the need for a twofold bias current.

This work moves the first steps toward a quantitative and physics-based analysis of the TCC VCSELs, consisting of the self-consistent solution of the optical, thermal and carrier transport effect. Such an approach is a fundamental tool to address the mentioned future challenges, providing deeper comprehension of the observations and narrowing down the technological parametric investigations.

One of the main results of this work is demonstrating the direct impact of the optical supermode features, namely, the frequency detuning and threshold gain splitting, on the PPR peak frequency and broadening. In this view, the formulation of novel design strategies of the resonator, aiming to control these parameters is going to play a starring role towards the next generation of TCC-VCSELs.

Appendix A
Derivation of a Multimode Rate Equation

This derivation aims at extracting a simple model for the multi-mode dynamics of a VCSEL starting from the solutions of a rigorous electromagnetic solver. We start with the inhomogeneous scalar wave equation [38]:

$$\nabla^2\mathcal{E}(\underline{r},t) - \mu_0\varepsilon(\underline{r})\partial_t^2\mathcal{E}(\underline{r},t) = \frac{1}{\varepsilon_0 \mathrm{c}^2}\partial_t^2\mathcal{P}(\underline{r},t), \qquad (10)$$

where $\mathcal{P}(\underline{r},t)$ is the polarization density vector, $\mathcal{E}(\underline{r},t)$ is the electric field, $\varepsilon(\underline{r})$ is the space-dependent refractive index profile, and μ_0 and c are the magnetic permeability of vacuum and the speed of light.

Usually, electromagnetic solvers compute the modes of a given geometry, which correspond to the solutions of the homogeneous wave (10):

$$e_i(t,\underline{r}) = \Psi_i(\underline{r})e^{\mathrm{i}\omega_{\mathrm{th}i}t}, \qquad \mathrm{i}\omega_{\mathrm{th}i} = -\frac{1}{2\tau_{\mathrm{p}i}} + \mathrm{i}\omega_i, \qquad (11)$$

where $\omega_{\mathrm{th}i}$ is the complex emission pulsation for the i-th mode, whose imaginary part is related to the photon lifetime $\tau_{\mathrm{p}i}$ and whose real part is related to the emission pulsation ω_i. We expand the time-dependent solution of the electrically pumped device on the basis of the cold-cavity modes as follows:

$$\mathcal{E}(\underline{r},t) = \sum_{i=1}^{N_{\mathrm{m}}} E_i(t)\Psi_i(\underline{r})e^{\mathrm{i}\omega_0 t}, \qquad \mathcal{P}(\underline{r},t) = P(\underline{r},t)e^{\mathrm{i}\omega_0 t} \qquad (12)$$

where N_{m} is the number of considered modes, ω_0 is an arbitrary real reference frequency, $E_i(t)$ are the complex mode amplitudes and $P(\underline{r},t)$ is the polarization density amplitude. We can define Ω_i as the complex difference between $\omega_{\mathrm{th}i}$ and ω_0:

$$\Omega_i = \mathrm{i}\omega_{\mathrm{th}i} - \mathrm{i}\omega_0 = \mathrm{i}\Delta\omega_i - \frac{1}{2\tau_{\mathrm{p}i}}, \qquad (13)$$

where $\Delta\omega_i = \omega_i$ - ω_0. We can assume that $E_i(t)$ is much slower than the reference optical carrier $e^{\mathrm{i}\omega_0 t}$ and that the emission frequencies of the modes are not too far from the reference frequency. This assumption can be expressed as:

$$(\mathrm{i}\omega_0+\Omega_i - \Omega_i)^2 \approx (\mathrm{i}\omega_{\mathrm{th}i})^2 - 2\mathrm{i}\omega_0\Omega_i, \quad |E_i(t)'| \ll \omega_0\,|E_i(t)|\,. \qquad (14)$$

Plugging (12) in (10), by evaluating the terms of the second derivative and simplifying the homogeneous solution for (11), assuming (14) and writing the expression of the polarization vector as a function of the electrical susceptibility χ yields:

$$\sum_{i=1}^{N_{\mathrm{m}}}[-\Omega_i E_i(t)\Psi_i(\underline{r}) + E_i'(t)\Psi\,(\underline{r})] = -\frac{\mathrm{i}\omega_0}{2\varepsilon_{\mathrm{r}}(\underline{r})}\chi(\underline{r},t)\mathcal{E}(t,\underline{r}). \qquad (15)$$

Now we can multiply the right and left-hand side of (15) by the complex conjugate of $\Psi_i^*(\underline{r})$ and then integrate over the space. Assuming that the susceptibility is zero outside the active region we can consider a constant value for ε_{r}. Also, we can write the susceptibility as a function of the carrier-dependent material gain as in [38]. Finally, exploiting the orthogonality of the modes we can write the expression for the i-th mode as follows:

$$\frac{\mathrm{d}}{\mathrm{d}t}E_i(t) = \Omega_i E_i(t) + \sum_{j=1}^{N_{\mathrm{m}}} k_{ij}E_j(t), \qquad (16)$$

with:

$$k_{ij} = \frac{v_{\mathrm{g}}\Gamma_{\mathrm{z}}}{2}\iint_{\mathrm{AR}} \Psi_i^*(\rho,\phi)g(\rho,\phi)\Psi_j(\rho,\phi)\,\mathrm{d}\rho\,\mathrm{d}\phi, \qquad (17)$$

where AR denotes the active region, v_{g} is the light velocity divided by the refractive index of the active region and g is a complex function that relates the material gain to the space-dependent carrier density N. In particular, the real part of g is related to light amplification, while the imaginary part is related to the refractive index variation [36], [42]. The system can be finally closed by introducing an equation for the carrier density and an expression for the complex gain.

Please notice that any offset in all the ω_i terms corresponds to a shift of the reference frequency, which is arbitrary, and therefore has no effect on the carrier and photon density. For this reason, it is possible to set an arbitrary ω_j to zero and set all the other $\omega_i = \Delta\omega_{ij}$ where $\Delta\omega_{ij}$ is the pulsation separation between the j-th and the i-th mode. Also, ω_i can be redefined as:

$$\omega_i \to \omega_i + \omega_{\mathrm{s}}, \qquad \omega_{\mathrm{s}} = -\frac{\alpha_{\mathrm{h}}}{2\tau_{\mathrm{p}1}}, \qquad (18)$$

where $\tau_{\mathrm{p}1}$ is the photon lifetime of the lasing mode. In this way, ω_1 can cancel out the imaginary part of the gain at the lasing condition, avoiding the computationally heavy time domain simulation of a high optical carrier. This choice can reduce the simulation time up to one order of magnitude.

*Disclosures:*The authors declare no conflicting interests.

References

[1] Ethernet Alliance, "2023 Ethernet Roadmap." 2023. Accessed: Dec. 11, 2023. [Online]. Available: https://ethernetalliance.org/technology/ethernet-roadmap/

[2] A. Liu, P. Wolf, J. A. Lott, and D. Bimberg, "Vertical-cavity surface-emitting lasers for data communication and sensing," *Photon. Res.*, vol. 7, no. 2, pp. 121–136, Feb. 2019.

[3] B. D. Padullaparthi, J. A. Tatum, and K. Iga, Eds., *VCSEL Industry - Communication and Sensing*, 1st ed. Hoboken, NJ, USA: Wiley, 2022.

[4] N. N. Ledentsov et al., "High speed VCSEL technology and applications," *J. Lightw. Technol.*, vol. 40, no. 6, pp. 1749–1763, Mar. 2022.

[5] M. Srinivasan et al., "End-to-end learning for VCSEL-based optical interconnects: State-of-the-art, challenges, and opportunities," *J. Lightw. Technol.*, vol. 41, no. 11, pp. 3261–3277, Jun. 2023.

[6] J. Wang et al., "100Gb/s PAM4 oxide VCSEL development progress at broadcom," *Proc. SPIE*, vol. 11300, pp. 84–89, 2020.

[7] U. Hecht et al., "Digital non-linear transmitter equalization for PAM-N-based VCSEL links enabling robust data transmission of 100 gbit/s and beyond," *MDPI Photon.*, vol. 10, no. 3, Mar. 2023, Art. no. 280.
[8] D. M. Kuchta et al., "A 50 Gb/s NRZ modulated 850 nm VCSEL transmitter operating error free to 90 °C," *J. Lightw. Technol.*, vol. 33, no. 4, pp. 802–810, Feb. 2015.
[9] J. Zhang et al., "PAM-8 IM/DD transmission based on modified lookup table nonlinear predistortion," *IEEE Photon. J.*, vol. 10, no. 3, Jun. 2018, Art. no. 7903709.
[10] H. Zhou et al., "Recent advances in equalization technologies for short-reach optical links based on PAM4 modulation: A review," *MDPI Appl. Sci.*, vol. 9, no. 11, Mar. 2019, Art. no. 2342.
[11] L. Minelli, F. Forghieri, A. Nespola, S. Straullu, and R. Gaudino, "A multi-rate approach for nonlinear pre-distortion using end-to-end deep learning in IM-DD systems," *J. Lightw. Technol.*, vol. 41, no. 2, pp. 420–431, Jan. 2023.
[12] A. Larsson, J. S. Gustavsson, A. Fülöp, E. Haglund, E. P. Haglund, and A. Kelkkanen, "The future of VCSELs: Dynamics and speed limitations," in *Proc. IEEE Photon. Conf.*, 2020, pp. 1–2.
[13] H. Dalir and F. Koyama, "29 GHz directly modulated 980 nm vertical-cavity surface emitting lasers with bow-tie shape transverse coupled cavity," *Appl. Phys. Lett.*, vol. 103, no. 9, 2013, Art. no. 091109.
[14] D. F. Siriani and K. D. Choquette, "Coherent coupling of vertical-cavity surface-emitting laser arrays," in *Advances in Semiconductor Lasers, Semiconductors and Semimetals Series*, vol. 86, J. J. Coleman, A. C. Bryce, and C. Jagadish, Eds. Amsterdam, Netherlands: Elsevier, 2012, ch. 6, pp. 227–267.
[15] S. T. M. Fryslie et al., "Modulation of coherently coupled phased photonic crystal vertical cavity laser arrays," *IEEE J. Select. Topics Quantum Electron.*, vol. 23, no. 6, pp. 1–9, Nov./Dec. 2017.
[16] E. Heidari, H. Dalir, M. Ahmed, V. J. Sorger, and R. T. Chen, "Hexagonal transverse-coupled-cavity VCSEL redefining the high-speed lasers," *Nanophotonics*, vol. 9, no. 16, pp. 4743–4748, 2020.
[17] H. Dalir and F. Koyama, "Bandwidth enhancement of single-mode VCSEL with lateral optical feedback of slow light," *IEICE Electron. Exp.*, vol. 8, no. 13, pp. 1075–1081, 2011.
[18] R. Lang and K. Kobayashi, "External optical feedback effects on semiconductor injection laser properties," *IEEE J. Quantum Electron.*, vol. 16, no. 3, pp. 347–355, Mar. 1980.
[19] M. Ahmed, A. Bakry, M. S. Alghamdi, H. Dalir, and F. Koyama, "Enhancing the modulation bandwidth of VCSELs to the millimeter-waveband using strong transverse slow-light feedback," *Opt. Exp.*, vol. 23, no. 12, pp. 15365–15371, 2015.
[20] S. Abdulrhmann, M. Ahmed, T. Okamoto, W. Ishimori, and M. Yamada, "An improved analysis of semiconductor laser dynamics under strong optical feedback," *IEEE J. Select. Topics Quantum Electron.*, vol. 9, no. 5, pp. 1265–1274, Sep./Oct. 2003.
[21] H. R. Ibrahim, M. S. Alghamdi, A. Bakry, M. Ahmed, and F. Koyama, "Modelling and characterisation of the noise characteristics of the vertical cavity surface-emitting lasers subject to slow light feedback," *Pramana–J. Phys.*, vol. 93, Aug. 2019, Art. no. 73.
[22] M. Ahmed and A. Bakry, "Modelling of semiconductor laser with double external cavities for use in ultrahigh speed photonics," *Pramana–J. Phys.*, vol. 95, May 2021, Art. no. 88.
[23] E. Heidari, M. Ahmed, H. Dalir, A. Bakry, A. Alshahrie, and V. J. Sorger, "VCSEL with multi-transverse cavities with bandwidth beyond 100 GHz," *Nanophotonics*, vol. 10, no. 14, pp. 3779–3788, 2021.
[24] U. Feiste, "Optimization of modulation bandwidth in DBR lasers with detuned bragg reflectors," *IEEE J. Quantum Electron.*, vol. 34, no. 9, pp. 2371–2379, Dec. 1998.
[25] A. Laakso and M. Dumitrescu, "Modified rate equation model including the photon–photon resonance," *Opt. Quantum Electron.*, vol. 42, pp. 785–791, Jun. 2011.
[26] M. Vallone, P. Bardella, and I. Montrosset, "Optimization of modulation bandwidth in DBR lasers with detuned Bragg reflectors," *IEEE J. Quantum Electron.*, vol. 47, no. 10, pp. 1269–1276, Oct. 2011.
[27] M. Yousefi and D. Lenstra, "Rate-equation description of multi-mode semiconductor lasers," *Proc. SPIE*, vol. 8980, pp. 57–75, 2014.
[28] T. Uusitalo, H. Virtanen, P. Bardella, and M. Dumitrescu, "Analysis of the photon–photon resonance influence on the direct modulation bandwidth of dual-longitudinal-mode distributed feedback lasers," *Opt. Quantum Electron.*, vol. 49, Jan. 2017, Art. no. 46.
[29] D. Chen, Y. Liu, and Y. Yu, "Understanding the photon-photon resonance of DBR lasers using mode expansion method," *Opt. Quantum Electron.*, vol. 55, Nov. 2022, Art. no. 29.
[30] W. North, N. Jahan, P. Strzebonski, and K. D. Choquette, "Modal characteristics of coupled vertical cavity surface emitting laser diode arrays," *J. Appl. Phys.*, vol. 132, no. 17, 2022, Art. no. 173102.
[31] P. J. Strzebonski, W. North, N. Jahan, and K. D. Choquette, "Analysis of coherence and coupling in vertical cavity surface emitting laser arrays," *IEEE J. Quantum Electron.*, vol. 58, no. 4, pp. 1–8, Aug. 2022.
[32] S. Hu and F. Koyama, "Coupled mode analysis of high-speed transverse coupled cavity vertical-cavity surface-emitting laser for low frequency chirp operations," *IEICE Electron. Exp.*, vol. 18, no. 13, pp. 1–5, 2021.
[33] M. Lindemann et al., "Coupled aperture VCSELs suitable for 100 GHz intensity modulation," in *Proc. 23rd Int. Conf. Transparent Opt. Netw.*, 2023, Art. no. We.C6.4.
[34] G. P. Bava, P. Debernardi, and L. Fratta, "Three-dimensional model for vectorial fields in vertical-cavity surface-emitting lasers," *Phys. Rev. A*, vol. 63, no. 2, 2001, Art. no. 23816.
[35] P. Debernardi and G. P. Bava, "Coupled mode theory: A powerful tool for analyzing complex VCSELs and designing advanced devices features," *IEEE J. Select. Topics Quantum Electron.*, vol. 9, no. 3, pp. 905–917, May/Jun. 2003.
[36] L. A. Coldren, S. W. Corzine, and M. L. Masanovic, *Diode Lasers and Photonic Integrated Circuits*, 2nd ed. New York, USA: Wiley, 2012.
[37] Y. Kominis, K. D. Choquette, A. Bountis, and V. Kovanis, "Antiresonances and ultrafast resonances in a twin photonic oscillator," *IEEE Photon. J.*, vol. 11, no. 1, Feb. 2019, Art. no. 1500209.
[38] F. Prati, A. Tesei, L. A. Lugiato, and R. J. Horowicz, "Stable states in surface-emitting semiconductor lasers," *Chaos Solitons Fractals*, vol. 4, no. 8–9, pp. 1637–1654, Aug. 1994.
[39] L. F. Shampine and M. W. Reichelt, "The MATLAB ODE suite," *SIAM J. Sci. Comput.*, vol. 18, no. 1, pp. 1–22, Jan. 1997.
[40] C. Chen, K. L. Johnson, M. Hibbs-Brenner, and K. D. Choquette, "Push-pull modulation of a composite-resonator vertical-cavity laser," *IEEE J. Quantum Electron.*, vol. 46, no. 4, pp. 438–446, Apr. 2010.
[41] H. Dalir, A. Matsutani, and F. Koyama, "Push-pull modulation of lateral coupling of dual VCSEL cavities using a bow-tie shape," *Proc. SPIE*, vol. 8639, pp. 244–250, Mar. 2013.
[42] G. Ghione, *Semiconductor Devices for High-Speed Optoelectronics*. Cambridge, U.K.: Cambridge Univ. Press, 2009.

Open Access funding provided by 'Politecnico di Torino' within the CRUI CARE Agreement